

TOI-3493 b: A planet with a Neptune-like density transiting a bright G0-type star

P. Chaturvedi^{1,2,*}, E. Goffo^{1,3}, D. Gandolfi³, C. M. Persson⁴, A. P. Hatzes¹, G. Nowak⁵, A. Bonfanti⁶, A. Bieryla⁷, W. D. Cochran^{8,9}, K. A. Collins⁷, S. B. Fajardo-Acosta¹⁰, S. B. Howell¹¹, J. M. Jenkins¹¹, J. Korth¹², J. Livingston^{13,14,15}, E. Pallé^{16,17}, S. N. Quinn⁷, R. P. Schwarz⁷, S. Seager^{18,19,20}, A. Shporer¹⁸, K. G. Stassun²¹, S. Striegel²², V. Van Eylen²³, C. N. Watkins⁷, J. N. Winn²⁴, and C. Ziegler²⁵

(Affiliations can be found after the references)

Received 18 December 2024 / Accepted 2 April 2025

ABSTRACT

We report the discovery of TOI-3493 b, a sub-Neptune-sized planet on an 8.15-d orbit transiting the bright ($V=9.3$) G0 star HD 119355 (aka TIC 203377303) initially identified by NASA's TESS space mission. With the aim of confirming the planetary nature of the transit signal detected by TESS and determining the mass of the planet, we performed an intensive Doppler campaign with the HARPS spectrograph, collecting radial velocity measurements. We found that TOI-3493 b lies in a nearly circular orbit and has a mass of $9.0 \pm 1.2 M_{\oplus}$ and a radius of $3.22 \pm 0.08 R_{\oplus}$, implying a bulk density of $1.47^{+0.23}_{-0.22} \text{ g cm}^{-3}$, consistent with a composition comprising a small solid core surrounded by a thick H/He-dominated atmosphere.

Key words. techniques: photometric – techniques: radial velocities – planets and satellites: detection – stars: individual: TOI-3493 – stars: solar-type

1. Introduction

Transiting planets are crucial for understanding planet formation and evolution, as their masses and radii can be precisely determined. They serve as test beds for transmission spectroscopy studies, providing insights into exoplanet atmospheres (see [Kreidberg 2018](#) and references therein). Initially, Jovian planets were the primary focus of characterization due to their detectability with both radial velocity (RV) and transit methods, ([Marcy et al. 2005](#); [Fischer et al. 2005](#); [Cumming et al. 2008](#); [Mayor et al. 2011](#); [Charbonneau et al. 2000](#)). However, advances in spectrographs on larger telescopes and the advent of space-based transit surveys such as CoRoT ([Baglin et al. 2006](#)), *Kepler* ([Borucki et al. 2010](#)), and TESS ([Ricker et al. 2015](#)) have led to the predominant discovery of small planets, with radii ranging in size from ones smaller than Neptune's to ones larger than Earth's'' ($R_p \approx 1\text{--}4.0 R_{\oplus}$).

Numerous studies have highlighted the abundance of small planets, which now constitute the majority of confirmed exoplanets ([Batalha et al. 2013](#); [Marcy et al. 2005](#); [Howard et al. 2010, 2012](#)). [Howard et al. \(2012\)](#) demonstrated that the planet occurrence rates per star, for planets that have orbital periods of less than 50 days, decrease from 0.130 ± 0.008 to 0.023 ± 0.003 as the planet radius increases from $2\text{--}4 R_{\oplus}$. Similarly, such an occurrence rate decreases to 0.013 ± 0.002 as the planet radius increases to $8\text{--}32 R_{\oplus}$. [Mulders et al. \(2015\)](#) observed that small planets are two to three times more common around M dwarfs than FGK-type stars. Another notable trend is the increase in the planet frequency with orbital separation from the host star up to a period of 10 days, beyond which the frequency stabilizes ([Howard et al. 2012](#); [Catanzarite & Shao 2011](#)).

Studies of small planets have revealed a bimodal radius distribution with a distinct gap, known as the radius valley

([Fulton et al. 2017](#); [Zeng et al. 2017](#); [Van Eylen et al. 2018](#); [Berger et al. 2018](#)). This gap suggests two distinct populations of exoplanets: one with Earth-like rocky cores with negligible atmospheres and the other with cores and H-He atmospheres. The radius valley, initially observed for solar-type stars, is believed to extend to planets around M dwarfs ([Van Eylen 2021](#)). Possible explanations for the gap include the photo-evaporation mechanism, whereby X-ray and ultraviolet (XUV) stellar insolation erodes hydrogen and helium atmospheres during formation ([Sanz-Forcada et al. 2011](#); [Owen & Wu 2013](#); [López & Fortney 2013](#)), and the formation of planets in environments with limited gas accretion during their formation process ([Owen & Wu 2013](#)). Additionally, core-powered mass losses from exoplanets may contribute to the radius valley phenomenon, particularly for young planets in close proximity to their host stars ([Ginzburg et al. 2018](#); [Gupta & Schlichting 2019, 2020](#)).

In this paper, we present the discovery of TOI-3493 b, a small exoplanet with a mass less than that of Neptune. We describe the properties of the host star in Sect. 2, followed by a detailed account of the data utilized for this study, including photometry data, HARPS spectroscopy, and high-resolution imaging data in Sect. 3. Section 4 outlines our methodology and results for determining the planetary and orbital parameters of the system. Finally, in Sect. 5, we interpret our findings, and in Sect. 6 we provide a concise summary.

2. Host star properties

TOI-3493 is a bright ($V=9.32$), G1/2V type star ([Houk & Smith-Moore 1988](#)). According to [Gaia Collaboration \(2021\)](#), the star is situated at a distance of about 96.76 ± 0.2 pc.

For the spectroscopic modeling of TOI-3493, we first analyzed our high-resolution co-added spectra with the software SpecMatch-Emp (SpecM; [Yee et al. 2017](#)), which compares

* Corresponding author; priyanka.chaturvedi@tifr.res.in

Table 1. Results from the spectroscopic modeling of TOI-3493 with Spectroscopy Made Easy (SME) and SpecMatch-Emp (SpecM) along with posteriors from the ARIADNE modeling of the SED.

Method	T_{eff} (K)	$\log g_{\star}$ (dex)	[Fe/H] (cgs)	$V \sin i$ (km s^{-1})
SME	5844 ± 42	4.25 ± 0.06	0.03 ± 0.04	2.2 ± 0.7
SpecM	5852 ± 110	4.25 ± 0.12	0.01 ± 0.09	...
ARIADNE	5851 ± 36	4.25 ± 0.07	0.02 ± 0.04	...

observations to a library of well-characterized stars with effective temperatures between 3000 and 7000 K. The results are listed in Table 1.

We then continued with detailed modeling with the Spectroscopy Made Easy¹ software (SME; Valenti & Piskunov 1996; Piskunov & Valenti 2017). This code computes synthetic spectra from atomic and molecular line data² (VALD; Ryabchikova et al. 2015) and stellar atmosphere grids that are fit to the observations for a chosen set of parameters. We used the SME version 5.2.2 and the Atlas12 atmosphere model (Kurucz 2013). We held the micro- and macro-turbulent velocities, V_{mic} and V_{mac} , fixed to 1.1 km s^{-1} (Brunt et al. 2008) and 3.8 km s^{-1} (Doyle et al. 2014), respectively. We modeled the spectral lines particularly sensitive to the fit parameters (one at a time). The procedure is described in detail in Persson et al. (2018). The results of the final model are in excellent agreement with SpecM and listed in Table 1. Both SpecM and SME point to a slightly evolved G1 star.

To obtain the stellar radius and mass, we used the derived spectroscopic parameters from SME as priors in modeling of the spectral energy distribution (SED) with the Python package ARIADNE³ (Vines & Jenkins 2022). We fit the broadband photometry bandpasses Johnson V and B (APASS), $GG_{\text{BP}}G_{\text{RP}}$ (DR3), JHK_S (2MASS), and WISE W1–W2, combined with the *Gaia* DR3 parallax. ARIADNE uses the dust maps of Schlegel et al. (1998) to put an upper limit of A_V . The software also allows fits based on four atmospheric model grids. For stars with temperatures above 4000 K, ARIADNE uses Phoenix v2 (Husser et al. 2013), BtSett1 (Allard et al. 2012), Castelli & Kurucz (2004), and Kurucz (1993) atmosphere models. The final radius was computed with Bayesian model averaging and we found that the Phoenix v2 has the highest probability (69%). The final stellar radius becomes $1.23 \pm 0.02 R_{\odot}$, the luminosity $1.6 L_{\odot}$, and the extinction is consistent with zero ($A_V = 0.02 \pm 0.02$). Finally, we obtained the stellar mass and age by interpolating the MIST (Choi et al. 2016) isochrones implemented in ARIADNE and found a stellar mass of $1.02 \pm 0.04 M_{\odot}$ and an age of $7.3 \pm 1.6 \text{ Gyr}$. Another estimate of the stellar mass was found by combining the radius and $\log g_{\star}$ which becomes $0.96 \pm 0.15 M_{\odot}$ in agreement with the mass from the MIST isochrones. We also note that the posteriors for the spectroscopic parameters from the ARIADNE model (listed in Table 1) are in excellent agreement with SME and Specmatch-emp. We plotted the SED of TOI-3493 and the resultant best-fitting Phoenix model with the ARIADNE software, as is shown in Fig. 1.

Finally, we used the empirically calibrated gyrochronology relations of Mamajek & Hillenbrand (2008) with the rotation period determined from the light curve as discussed in Sect. 4.1.1, together with the stellar T_{eff} , giving an estimated

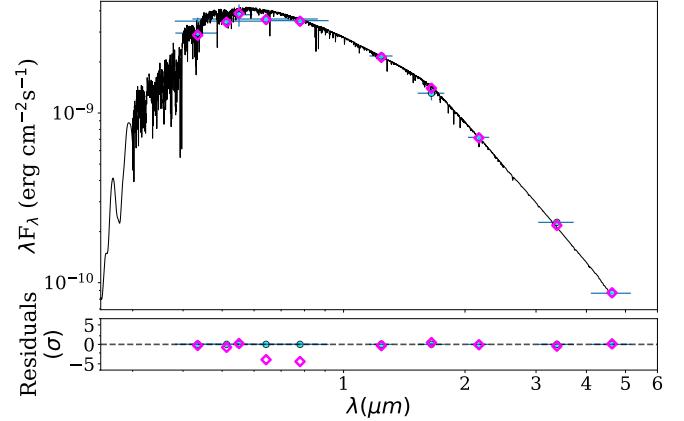


Fig. 1. Spectral energy distribution of TOI-3493 and the best-fitting model (Phoenix v2, Husser et al. 2013) with the ARIADNE software. The magenta diamonds mark the synthetic photometry, while the observed photometry is shown in blue points. The vertical error bars are the 1σ uncertainties of the magnitudes, and the horizontal bars are the effective width of the photometric passbands. The lower panel shows the residuals normalized to the errors of the photometry; hence, the largest relative errors are from *Gaia* DR3.

Table 2. Stellar parameters of TOI-3493.

Parameter	Value	Reference
<i>Name and identifiers</i>		
Name	HD 119355	HD1920
TOI	3493	ExoFOP-TESS
TIC	203377303	Sta18
<i>Coordinates and basic photometry</i>		
α (J2016.0)	13:43:11.72	<i>Gaia</i> DR3
δ (J2016.0)	−22:35:06.48	<i>Gaia</i> DR3
G (mag)	9.127 ± 0.0027	<i>Gaia</i> DR3
J (mag)	8.127 ± 0.018	Cut03
H (mag)	7.891 ± 0.017	Cut03
K (mag)	7.776 ± 0.026	Cut03
<i>Parallax and kinematics</i>		
π (mas)	10.29 ± 0.02	<i>Gaia</i> DR3
d (pc)	96.76 ± 0.2	<i>Gaia</i> DR3
$\mu_{\alpha} \cos \delta$ (mas a ^{−1})	43.32 ± 0.02	<i>Gaia</i> DR3
μ_{δ} (mas year ^{−1})	$−72.24 \pm 0.015$	<i>Gaia</i> DR3
<i>Photospheric parameters and spectral type</i>		
Sp. type	G1/2 V	Houk88
T_{eff} (K)	5844 ± 42	This work
$\log g$	4.25 ± 0.06	This work
[Fe/H]	0.03 ± 0.04	This work
$v \sin i$ (km s^{-1})	2.2 ± 0.7	This work
<i>Stellar properties</i>		
M_{\star} (M_{\odot})	1.023 ± 0.041	This work
R_{\star} (R_{\odot})	1.228 ± 0.017	This work
age	7.3 ± 1.67	This work
$P_{\text{rot;GP}}$ (d)	37.4 ± 1.5	This work ^(a)

Notes. *Gaia* DR3: Gaia Collaboration (2020); HD1920: Cannon & Pickering (1920); Houk88: Houk & Smith-Moore (1988); EXOFOP: <https://exofop.ipac.caltech.edu/>; Sta18: Stassun et al. (2018); Sta19: Stassun et al. (2019). ^(a)See Sect. 4.1.1 for a P_{rot} determination.

¹ <http://www.stsci.edu/~valenti/sme.html>

² <http://vald.astro.uu.se>

³ <https://github.com/jvines/astroARIADNE>

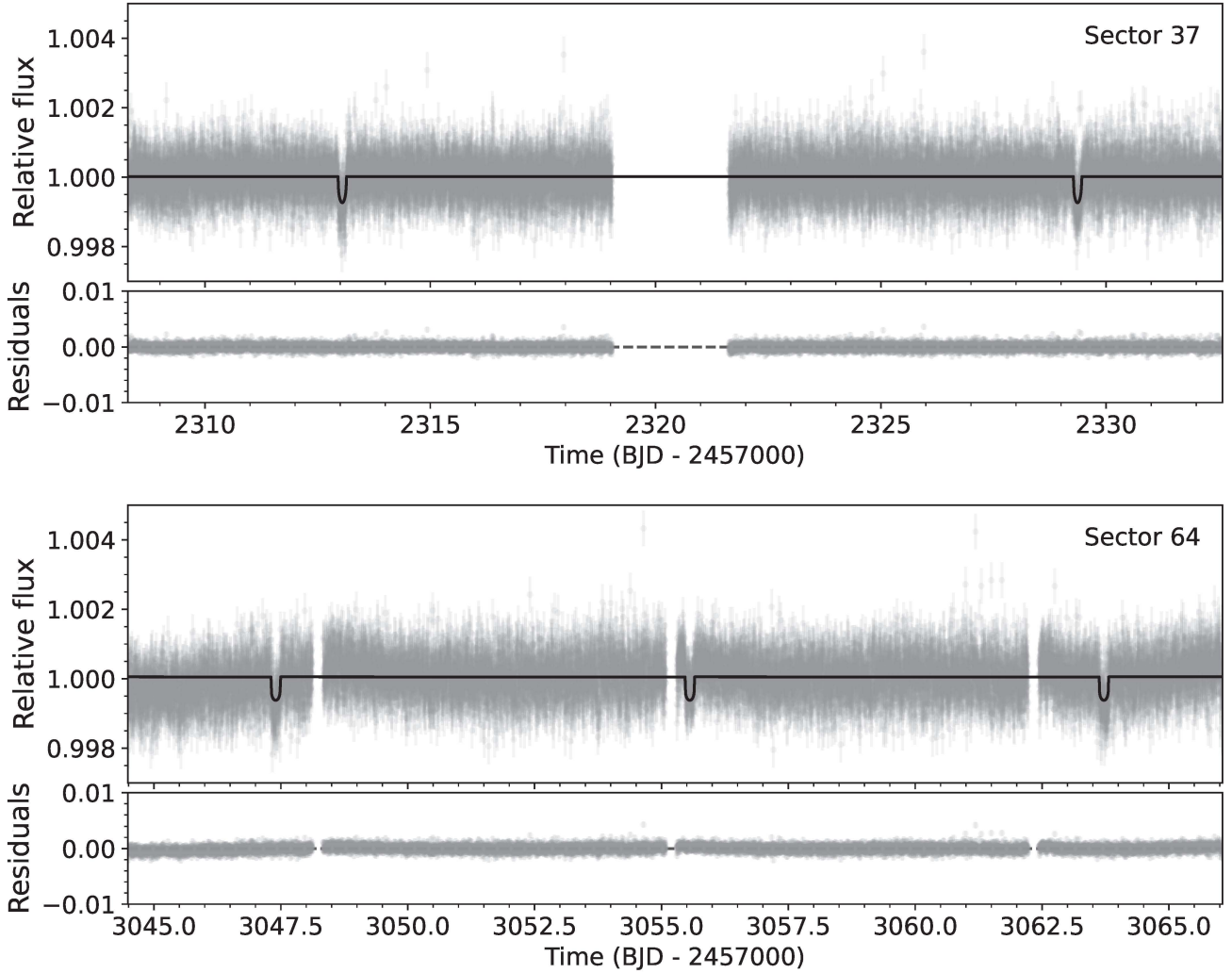


Fig. 2. TESS PDCSAP light curve for TOI-3493 (gray points) for two sectors, 37 (top) and 64 (bottom), overplotted with the transiting-planet model in black.

system age of 8.5 ± 0.6 Gyr, consistent with the age estimated above. Table 2 summarizes the stellar parameters of TOI-3493 with their corresponding uncertainties and references.

3. Observations and data acquisition

3.1. Transit detection

3.1.1. TESS photometry

The Transiting Exoplanet Survey Satellite (TESS) mission, equipped with four $2k \times 2k$ CCD cameras, each covering a 24×24 deg² field of view, has been pivotal in the discovery of numerous exoplanet candidates spanning a range of sizes and orbital separations. The Mikulski Archive for Space Telescopes (MAST)⁴ is tasked with archiving both raw and processed light curves pertaining to the observed candidates.

TOI-3493, also designated TIC 203377303, was observed at a 2 minute cadence in Sector 37 in April 2021 and the image data were reduced and analyzed by the Science Processing Operations Center (SPOC; Jenkins et al. 2016) at NASA Ames Research Center. The data validation report (Twicken et al. 2018; Li et al. 2019) attributed a TESS magnitude of 8.7 to the candidate.

⁴ <https://mast.stsci.edu>, <https://archive.stsci.edu/>

According to the difference image centroid tests from the Sector 37 – Sector 64 multisector search, the host star is located within 1.93 ± 2.60 arcsec of the source of the transit signal source of TOI-3493.

The SPOC conducted a transit search of Sector 37 on 4 June, 2021, with an adaptive noise compensating filter (Jenkins 2002; Jenkins et al. 2010, 2020), producing a TCE for which an initial limb darkened transit model was fit (Li et al. 2019) and a series of diagnostic tests were conducted to help make or break the planetary nature of the signal (Twicken et al. 2018). The TESS Science Office (TSO) reviewed the vetting information and issued an alert on 21 June, 2021 (Guerrero et al. 2021). The TESS SPOC (Jenkins et al. 2016) identified a transit signal with a periodicity of 16.32 d. Each TESS sector observes its designated field of view for approximately 27 d, allowing for a data downlink. However, during sector 37, a data pause lasting 1.19 d occurred, during which a transit of our target took place. This anomaly led to an erroneous determination of the orbital period in sector 37 data, a discrepancy rectified by additional observations conducted during sector 64 in April 2023. All TESS observations for this source are listed in Table 3. The signal was also recovered as additional observations were made in sector 64, and the transit signature passed all the diagnostic tests presented in the data validation reports. Subsequent analysis revised the orbital

Table 3. TESS observations of TOI-3493.

Sector	Camera	Cycle	Start date	End date
37	1	3	3 April 2021	28 April 2021
64	1	6	6 April 2023	1 May 2023

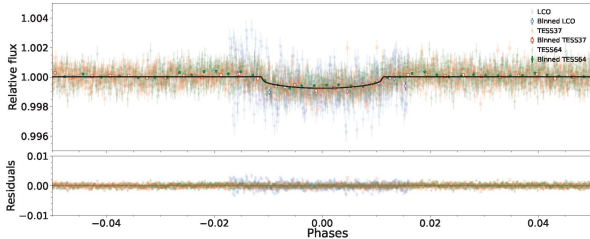


Fig. 3. Phase-folded TESS and LCOGT transit light curves for TOI-3493 b at 8.15 d. Gray circles are LCO observed points, red squares and green stars are 2 minute cadence TESS data for sectors 37 and 64, respectively, and darker shades of the same color are binned data for respective datasets (shown only for reference; unbinned points were used to fit the model). The best-fit *juliet* model (black line; see Sect. 4) is overplotted for TOI-3493 b.

period to 8.157 d, with a transit depth of 763.88 parts per million (ppm) and a transit duration of 4.4 h, corresponding to a planetary radius of $3.39 R_{\oplus}$ for TOI-3493 b.

We extracted data for SPOC pre-search data conditioning simple aperture photometry (PDCSAP; Smith et al. 2012; Stumpe et al. 2012, 2014) for TOI-3493 from sectors 37 and 64. The planet’s detection at an 8.17 d period is confirmed in Fig. 2. Phase-folded data and the best-fit model for the planet in both sectors are presented in Fig. 3 (see Sect. 4.2.3 for a detailed analysis description).

Given the relatively large pixel size of $\sim 21''$ in the TESS imagery, there exists a possibility of contamination from nearby stars affecting the host star. In particular, the *Gaia* G_{RP} band (630–1050 nm) and the TESS T band (600–1000 nm) share overlapping wavelength coverage. To assess potential contamination, we overlaid all nearby *Gaia* sources against the TESS aperture as a reference for the observed field of view, as is shown in Fig. 4. Notably, no sources exhibit a magnitude difference within 6 of that of TOI-3493, with only a few stars displaying a magnitude contrast of 8 or higher. The TIC contamination of the source is estimated at $\sim 0.43\%$, indicating that more than 99% of the flux within the photometric aperture originates from the source. In addition, we performed high-resolution imaging analysis, described in Sect. 3.3, to mitigate the influence of nearby neighbors.

3.1.2. LCOGT light curve follow-up

The pixel scale of the TESS is approximately $21''$ per pixel, with photometric apertures typically extending out to roughly $1'$, often leading to the blending of multiple stars within the TESS aperture. To mitigate the possibility of a nearby eclipsing binary (NEB) blend being the source of the TESS detection and to attempt on-target event detection, we conducted observations of TOI-3493 as part of the TESS Follow-up Observing Program⁵ Sub Group 1 (TFOP; Collins 2019). All light curve data are

accessible on the EXOFOP-TESS website⁶. All the observations conducted as a part of this programme are described in Table 4.

We observed transit windows of TOI-3493 b on 29 June, 2021, UT and 4 March, 2024, UT in the Pan-STARRS z -short band using the Las Cumbres Observatory Global Telescope (LCOGT; Brown et al. 2013) 1.0 m network node at Cerro Tololo Inter-American Observatory in Chile (CTIO). The images were calibrated by the standard LCOGT BANZAI pipeline (McCully et al. 2018) and differential photometric data were extracted using *AstroImageJ* (Collins et al. 2017).

TOI-3493 was intentionally saturated on 29 June, 2021, UT to better measure the light curves of the fainter nearby stars to improve the check for an NEB. We extracted light curves for all eight *Gaia* DR3 and TICv8 neighboring stars within $2'5$ of TOI-3493 that are bright enough in TESS band to produce the TESS detection (allowing for the magnitude to be an extra 0.5 fainter in the TESS band in an attempt to accommodate uncertainties). We thus checked all stars down to 8.3 magnitudes fainter than TOI-3493 (i.e., down to 17.0 mag in TESS band). We calculated the root mean square (RMS) of each of the eight nearby star light curves (binned in 5 minute bins) and found that the values are smaller by at least a factor of 5 compared to the expected NEB depth in each respective star. We then visually inspected the light curves to ensure no obvious deep eclipse-like signal existed. We therefore rule out a NEB blend as the cause of the TOI-3493 b detection in the TESS data.

The exposure time for the observation on 4 March 2024, UT was optimized for TOI-3493 photometry and was mildly defocused in an attempt to improve photometric precision for the purposes of detecting the shallow transit event on TOI-3493. Circular photometric apertures with radius $7'8$ (20 pixels) were used to extract the TOI-3493 differential light curve using eight reference stars. The apertures exclude the flux from all neighbors reported in the *Gaia* DR3 catalog. Telescope guiding was not precise during the observation, so target star centroid location linear detrending was applied, which removed most of the light curve trend. Target star full-width-at-half-maximum (FWHM) and sky-background detrending were also justified by the Bayesian information criterion and were applied to remove further transit model residuals. The transit detection from LCOGT along with the TESS data is shown in Fig. 3.

3.2. High-resolution spectroscopy

We used the High Accuracy Radial velocity Planet Searcher (HARPS) spectrograph (Mayor et al. 2003) to measure precise RVs for the target. A total of 83 high-resolution spectra, spanning from 16 February, 2022, to 17 August, 2023 (UT), were acquired as part of our extensive observing campaigns 106.21TJ.001 and 1102.C-0923, dedicated to the follow-up of TESS transiting planets (PI: D. Gandolfi). These spectra were obtained at a resolving power of $R \approx 115\,000$, covering the wavelength range of 378–691 nm, with exposure times ranging between 1200 and 1800 s, contingent upon prevailing sky and seeing conditions. The median signal-to-noise ratio (S/N) of the processed spectra is approximately 86 per pixel at 550 nm.

Data reduction of the HARPS spectra was carried out using the dedicated data reduction software DRS (Lovis & Pepe 2007; Pepe et al. 2002), facilitating the extraction of absolute RV measurements by cross-correlating the echelle spectra of TOI-3493 with a G2 numerical mask (Baranne et al. 1996). Furthermore, the DRS was utilized to derive the Ca II H & K lines activity

⁵ <https://tess.mit.edu/followup>

⁶ <https://exofop.ipac.caltech.edu/tess/target.php?id=203377303>

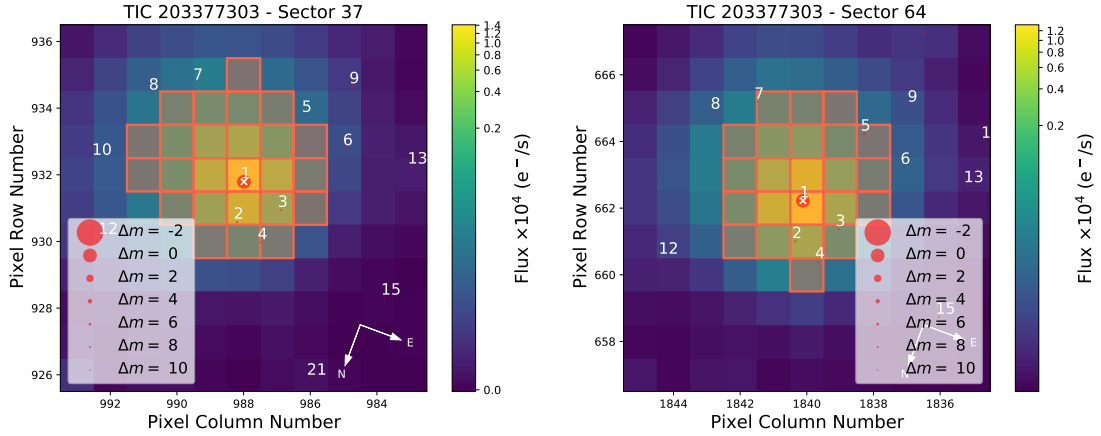


Fig. 4. Target pixel files of TOI-3493 in TESS sectors 37 (left) and 64 (right). The electron counts are color-coded. The red-bordered pixels are used in the simple aperture photometry. TOI-3493 is represented with a circle marked with #1. The other stars are represented with red circles and the size of the circle related to the magnitude difference. The other stars in the field are relatively faint, and hence appear as tiny dots.

Table 4. Ground-based observations of TOI-3493 transits.

Telescope	Camera or instrument	Filter	Pixel scale (arcsec)	PSF ^(a) (arcsec)	Aperture radius (pixel)	Date (UT)	Duration (min)
LCO-SSAO (1.0 m)	Sinistro	z_s	0.389	4.03	18.0	05-04-2023	363.0
LCO-SAAO (1.0 m)	Sinistro	z_s	0.389	3.17	17.0	04-04-2023	537.0
LCO-SSO (1.0 m)	Sinistro	z_s	0.389	3.3	16.0	19-03-2023	463.0
LCO-CTIO (1.0 m)	Sinistro	z_s	0.389	1.7	12.0	29-06-2021	258.0

Notes. ^(a)Estimated point spread function.

indicator ($\log R'_{\text{HK}}$), as well as the bisector inverse slope (BIS), FWHM, and contrast of the cross-correlation function (CCF). Relative RV measurements and supplementary activity indicators ($H\alpha$ and Na D lines) were also extracted by employing the Template Enhanced Radial velocity Re-analysis Application (TERRA; [Anglada-Escudé & Butler 2012](#)).

The absolute DRS and relative TERRA RV measurements of TOI-3493, along with the corresponding activity indicators, are presented in Table B.1. One HARPS spectrum⁷ exhibited an anomalously low S/N at wavelengths below ~ 450 nm, likely attributable to misalignment of the HARPS fiber relative to the stellar photo center during exposure. Consequently, this spectrum was deemed unsuitable for analysis, and its associated RV and activity index values are omitted from Table B.1.

3.3. High-resolution imaging

The *Gaia* DR3 renormalized unit weight error (RUWE) value for TOI-3493 is 1.1, much below 1.4, which is considered a critical value to distinguish between single and multiple sources ([Arenou et al. 2018](#); [Lindegren et al. 2018](#)). We used the high-resolution imaging facilities at our discretion to confirm the nature of the target source, as is described in the following subsections.

3.3.1. Gemini

If an exoplanet host star has a spatially close companion, that companion (bound or line of sight) can create a false-positive transit signal if it is, for example, an eclipsing binary (EB) or

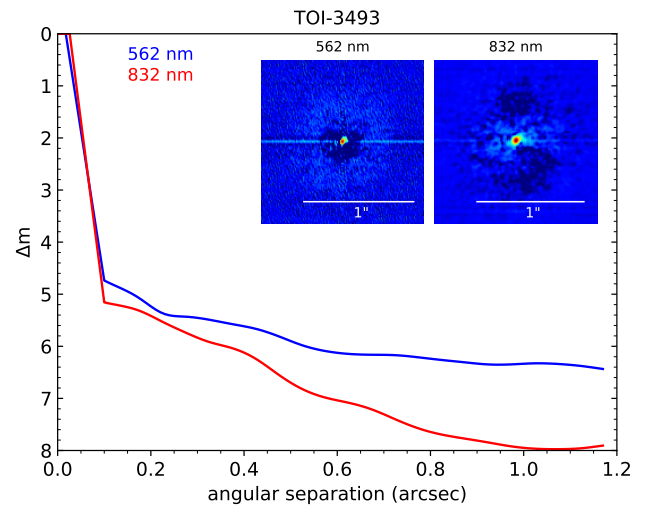


Fig. 5. Reconstructed image of TOI-3493 from Zorro speckle instrument on the Gemini South 8-m telescope. The figure includes the 5σ contrast curves for the simultaneous observations at 562 nm (blue) and 832 nm (red).

another form of variable star. “Third-light” flux from the close companion star leads to an underestimated planetary radius if not accounted for in the transit model ([Ciardi et al. 2015](#)) and causes non-detections of small planets residing with the same exoplanetary system ([Lester et al. 2021](#)). Additionally, the discovery of close, bound companion stars, which exist in nearly one half of FGK-type stars ([Matson et al. 2018](#)) and less frequently for M-type stars, provides crucial information for our understanding of

⁷ Root file name: HARPS.2023-02-03T07:31:42.961.

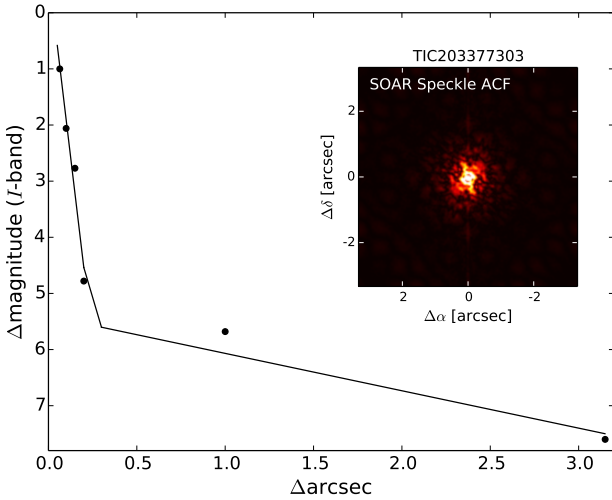


Fig. 6. SOAR image of TOI-3493 and contrast curve (5σ limits in black dots, rms dispersion in magenta).

exoplanetary formation, dynamics, and evolution (Howell et al. 2021). Thus, to search for close-in bound companions that are unresolved in TESS, we obtained high-resolution speckle imaging observations of TOI-3493. TOI-3493 was observed on May 17, 2022, UT using the Zorro speckle instrument on the Gemini South 8-m telescope⁸. Zorro provides simultaneous speckle imaging in two bands (562 nm and 832 nm) with output data products including a reconstructed image with robust contrast limits on companion detections (Scott et al. 2021; Howell & Furlan 2022). Three sets of 1000×0.06 s exposures were collected and subjected to Fourier analysis in our standard reduction pipeline (see Howell et al. 2011). Figure 5 shows our final contrast curves and the reconstructed speckle images. We find that TOI-3493 is a single star revealing no close companions brighter than 5–8 magnitudes below that of the target star from the diffraction limit (20 mas) out to $1.2''$. At the distance of TOI-3493 ($d=97$ pc), these angular limits correspond to spatial limits of 2 to 116 au.

3.3.2. SOAR

High-angular-resolution imaging is needed to search for nearby sources that can contaminate the TESS photometry, resulting in an underestimated planetary radius, or that can be the source of astrophysical false positives, such as background eclipsing binaries. We searched for stellar companions to TOI-3493 with speckle imaging on the 4.1-m Southern Astrophysical Research (SOAR) telescope (Tokovinin 2018) on 14 July, 2021, UT, observing in the Cousins I band, a similar visible bandpass to TESS. This observation was sensitive to a 5.7-magnitude fainter star at an angular distance of $1''$ from the target. More details of the observations within the SOAR TESS survey are available in Ziegler et al. (2020). The 5σ detection sensitivity and speckle autocorrelation functions from the observations are shown in Fig. 6. No nearby stars were detected within $3''$ of TOI-3493 in the SOAR observations.

⁸ <https://www.gemini.edu/sciops/instruments/alopeke-zorro/>

4. Analysis and results

4.1. Investigating the periodic signals

The periodic signals evident in both the RV and photometry data of the star may arise from intrinsic stellar activity, such as dark spots, bright faculae, and magnetic fields, which manifest as periodically modulated signals in long baseline photometry data. Consequently, we conducted separate investigations of the spectroscopic and photometric data.

4.1.1. Photometry data

To probe stellar activity induced phenomena, we analyzed archival photometry data obtained from the SuperWASP mission, accessible through the SuperWASP consortium via the NASA Exoplanet Archive⁹. The SuperWASP project comprises two robotic observatories situated in the northern and southern hemispheres, each equipped with eight cameras boasting a broad field of view of 7.8×7.8 deg² per camera (Butters et al. 2010). TOI-3493 was included in the photometric observations conducted by SuperWASP-South, situated at the South African Astronomical Observatory (SAAO). These observatories are designed to conduct systematic sky monitoring for photometric phenomena. Observations of TOI-3493 spanned from May 2006 to August 2014, yielding approximately 10 000 measurements. The data were acquired using a broadband filter with a passband spanning from 400 nm to 700 nm.

We conducted a generalized Lomb–Scargle (GLS) periodogram analysis (Zechmeister & Kürster 2009) to the SuperWASP data. The GLS periodogram shows a strong peak at 41 d, with subsequent peaks occurring at 30, 34, and 47 d, as is shown in the left panel of Fig. 7. Due to a large number of significant peaks occurring in the periodogram, we employed a Gaussian process (GP) model, implemented via the fitting tool juliet (Espinoza et al. 2019), to analyze the SuperWASP light curves. The data were nightly binned to mitigate short-period variations, and we utilized the built-in quasi-periodic (QP) kernel of the Python library george (Ambikasaran et al. 2015). Mathematically, this kernel combines an exponential-squared component with a sinusoidal component, expressed as

$$k(\tau) = \sigma_{\text{GP}}^2 \exp\left(-\alpha \text{GP}\tau^2 - \Gamma \sin^2\left[\frac{\pi\tau}{P_{\text{rot;GP}}}\right]\right), \quad (1)$$

where σ_{GP} denotes the GP amplitude (in ppm), Γ represents the dimensionless amplitude of the GP sine-squared component, α indicates the inverse length scale of the GP exponential component (in days⁻²), τ signifies the time lag (in days), and $P_{\text{rot;GP}}$ denotes the rotational period of the star (in days). While the sinusoidal signal associated with active regions on the star may vary over time (Angus et al. 2018), the QP kernel offers an effective means of modeling such intricate periodic behaviors.

We treated data from each camera as originating from distinct instruments to avoid potential instrumental offsets across datasets. To account for relative flux offsets between different instruments, we assumed a normal distribution ranging from 0 to 1000. The uninformative priors were applied to all parameters: σ_{GP} (uniform distribution between 10^{-8} ppm and 10^8 ppm), Γ (uniform distribution between 10^{-6} and 10^6), instrumental jitter (uniform distribution between 0.1 ppm and 10^9 ppm), α (uniform between 10^{-10} d⁻² and 1 d⁻²), and $P_{\text{rot;GP}}$ (uniform between 10

⁹ <https://exoplanetarchive.ipac.caltech.edu/docs/SuperWASPmission.html>

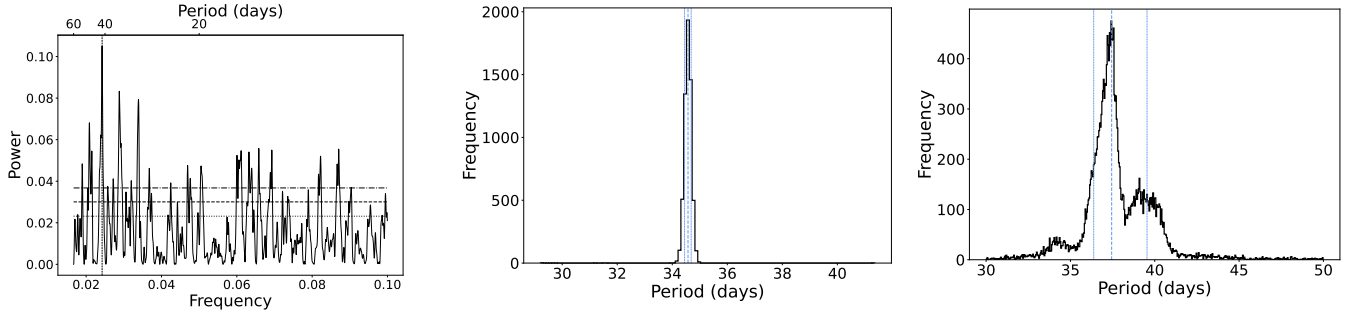


Fig. 7. Rotational period of TOI-3493 determined through photometry and spectroscopy data described in the following panels. (Left) GLS periodogram for the SuperWasp data plotted, with a significant peak occurring at 41 d and several secondary peaks occurring between 30–50 d. The false alarm probabilities at 0.1%, 1%, and 10% are plotted from top to bottom. (Middle) PDF for the most significant period at 34.5 d by modeling the nightly binned photometric SuperWASP data with GPs. (Right) PDF for the estimated rotational period of the star, while modeling the RV data with GPs. The PDF has a peak at 37.4 ± 1.5 d followed by a small peak centered at 39 d.

and 60 d). The rotational period, determined from the GP analysis, was found to be $P_{\text{rot;GP}} = 34.6 \pm 0.1$ d, as is seen from the peak of the posterior distribution function (PDF) seen in the middle panel of Fig. 7.

4.1.2. Spectroscopy data

We conducted a GLS periodogram analysis (Zechmeister & Kürster 2009) on the HARPS RV data for TOI-3493, alongside its associated activity components extracted from the data. The GLS periodogram of the RV data along with the activity indicators are displayed in Fig. 8. Followed vertically by the RV panel on top are the activity indicators encompassing the FWHM of the CCF, BIS, contrast, $H\alpha$ activity indicator, $\log R'_{HK}$, S-index, Na ID₁, NaI D₂, and the window function in each panel, respectively.

We pre-whitened the data by sinusoidal fitting and subtracting the prominent 8.15 d signal evident in the RV data. Subsequent examination of the RV periodograms, in comparison to other activity indicators, reveals no conspicuous signal at the 8.15 d, accompanied by additional features between 34 and 41 d and in some cases around 50 d. The contrast activity indicator exhibits a prominent signal at half of this period, namely 20 d. Similarly, analysis of other indicators such as $H\alpha$ reveals a peak occurring around 37 d. The activity indices, alongside their associated uncertainties, are detailed in Table B.1.

While modeling the RV data, as is discussed in Sect. 4.2.2, for its planetary signal, an additional component in the form of GPs was introduced to account for the residual peaks observed in the RV data. These peaks overlap with some of the activity indicator indices shown in Fig. 8. The period derived from the GP reflects the rotational modulation of the star. The PDF exhibits a primary peak at 37.4 ± 1.5 d, along with a secondary, broader peak around 39 d, as is illustrated in the right panel of Fig. 7.

The 41 d signal, observed as the strongest peak in the GLS periodogram (left panel), and the 34 d signal, identified through GP modeling of the photometry data (middle panel), are found to be one-year (365 d) aliases of the 37.4 d signal. Therefore, based on a comprehensive analysis of the periodic signals seen in both the photometric and spectroscopic data, we conclude that the rotational period of the star is 37.4 ± 1.5 d.

4.2. Orbital parameters for TOI-3493 system

Modeling the RV and transit data of a system allows for the determination of crucial parameters, such as the radius, mass,

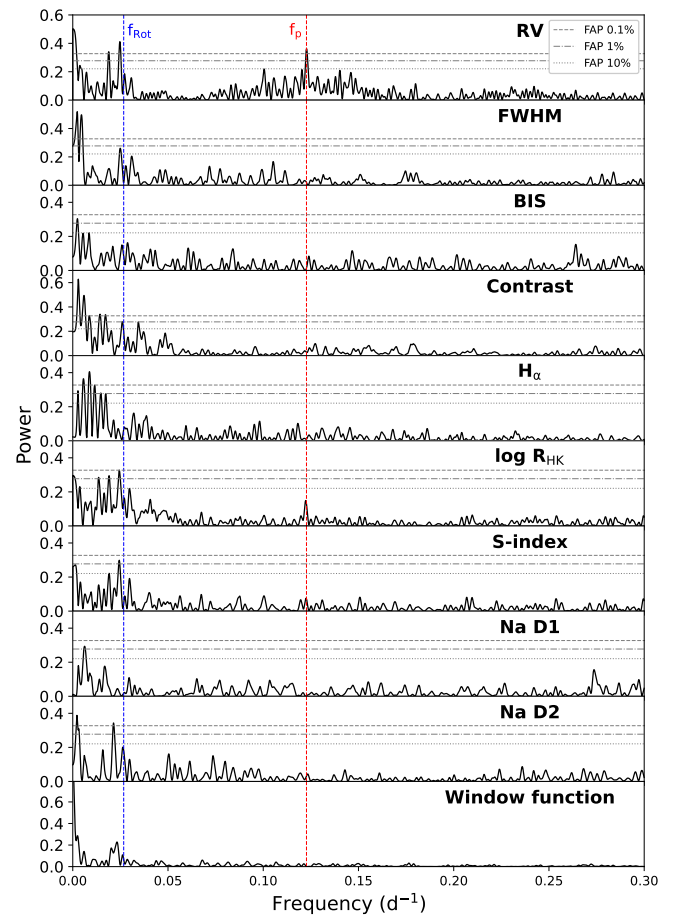


Fig. 8. GLS periodograms of various parameters derived from the HARPS data: RV measurements, FWHM of the CCF, BIS, contrast, $H\alpha$ index, $\log R'_{HK}$ index, S-index, Na ID₁, and NaI D₂, juxtaposed with the respective window function to scrutinize potential alias signals. A vertical red line is annotated to denote the frequency corresponding to the period of the planet (8.15 d), and the blue line corresponds to the rotational period of the star (37.4 d).

and bulk density of the transiting planet, along with its orbital parameters, such as the inclination and eccentricity. We utilized the Python-based library *juliet* to model all available transit and RV data. *juliet* employs the nested sampling algorithm from *dynesty* (Speagle 2020) to compute the Bayesian

model log evidence, $\ln \mathcal{Z}$, along with its posterior distribution. This library relies on other Python packages such as `radvel` (Fulton et al. 2018) for RV modeling and `batman` (Kreidberg 2015) for transit modeling. To account for nonperiodic variations, GPs are incorporated into the modeling through packages such as `george` (Ambikasaran et al. 2015) and `celerite` (Foreman-Mackey et al. 2017). The modeling of the TOI-3493 system was conducted in three steps, outlined below.

4.2.1. Modeling the transit data only

The TESS data for TOI-3493 was available for two TESS sectors, 37 and 64, from which the PDCSAP light curves were retrieved. Using the SPOC reported period of 16.32 d and ephemeris as priors, we initially attempted to fit a 16.32 d period to the dataset. However, the RV data indicated a strong peak at 8.15 d instead of 16.32 d, prompting us to refine our transit search at half the quoted period, at 8.15 d. There are systematic gaps in the TESS data due to the data downlink time. A transit occurred during one the gaps for the TOI-3493 system resulting in an incorrect reported period. We let the transiting planet have a uniform period prior between 7.5 to 9 d. We chose the same transit center time as mentioned by SPOC but also kept the prior information with a uniform distribution ranging from BJD 2459310.0 to BJD 2459314.0.

The stellar density (ρ_*) was utilized as a free parameter instead of the scaled stellar radius (a/R_*). As was discussed in Sozzetti et al. (2007), fitting for the ρ_* is considered a better choice as it incorporates information from both stellar mass and radius. We also allowed the ρ_* prior to have a uniform distribution with a wide range of possible choices between 100 and 10 000 kg m⁻³. The planet-to-star ratio (p_1) and impact parameter (b_1) were parameterized based on Espinoza (2018), with other parameters set within appropriate ranges. The successful execution of the script allowed us to derive the orbital period (P_b) and central transit times (t_{0b}), which were subsequently used as priors for simultaneous data fitting. The parameters that are better determined through RV such as eccentricity–omega ($e-\omega$) were fixed at 0 and 90°, respectively, for this step. In the absence of any close known companions, discussed in Sect. 3.3, we fixed the dilution factor to 1.0. We chose quadratic limb darkening law with parameters varying uniformly between 0 and 1. The flux offset had a normal distribution around 0 with a 0.1 width in units of normalized flux. We set the priors for the flux scatter to vary uniformly between 10⁻⁵ to 10⁵ ppm. The successful execution of the script let us derive the orbital period, P_b , as 8.1594647^{+0.0000584}_{-0.0000554} d and the central transit times, t_{0b} , as BJD 2459313.0472^{+0.0030}_{-0.0023}. These parameters were used as priors when we fit the data simultaneously as is discussed in Sect. 4.2.3.

4.2.2. Modeling the RV data only

The preliminary analysis of the HARPS RV data, using the GLS periodogram, facilitated the determination of the correct orbital period for the transiting planet orbiting TOI-3493. Contrary to the 16.32 d period reported by the TESS mission’s SPOC, we identified a period of 8.15 d (Jenkins et al. 2016) for the planetary transit. This was corroborated by independent transit modeling efforts detailed in Sect. 4.2.1. Subsequent to the removal of the planetary signal at 8.15 d, a prominent RV signal emerged at 37 d, accompanied by residuals at periods of 34, 41, and 52 d. These residual periods are related to the stellar rotational period and its alias, as is discussed in Sect. 4.1.1.

Table 5. Comparison of RV-only models.

Models	$\ln \mathcal{Z}$	$ \Delta \ln \mathcal{Z} $
<i>Two-signal models (without activity modeling)</i>		
1cp	-227.77	7.76
1ep	-238.57	18.56
2cp	-220.02	0
1cp+1ep	-230.38	10.37
2ep	-233.95	13.94
1cp+1t	-216.75	-3.26
1cp+qt	-229.98	9.96
2cp+1t	-219.09	-0.93
2cp+qt	-219.29	-0.72
1cp+GP	-205.21	-14.80
1ep+GP	-209.53	-10.49

Notes. Here, “cp,” “ep,” “t,” “qt,” and “GP” refer to a circular planet model, eccentric planet model, linear trend, quadratic trend, and GPs, respectively. $\ln \mathcal{Z}$ and $|\Delta \ln \mathcal{Z}|$ are the log-evidence and relative absolute log-evidence with respect to the fiducial model (2cp here), respectively.

We initiated our modeling process by fitting the transit data assuming a circular orbit, denoted as the “1cp model.” Using the derived values of P_b and t_{0b} from the transit-only best-fit (Sect. 4.2.1), we varied the semi-amplitude for the RV between 0 and 50 m s⁻¹ with a uniform distribution. The instrument offset parameter was kept uniform between -10 and 10 m s⁻¹, and the RV jitter was varied between 0.01 and 10 m s⁻¹ with a log uniform distribution. For circular (cp) models, the eccentricity (e) and argument of periastron (ω) were fixed at 0 and 90, respectively. In cases in which circular models were not fit, denoted as Keplerian (ep) models, the parameters were parameterized accordingly (Espinoza et al. 2019).

We assessed various models against the RV data, employing the selection criteria by Trotta (2008) to discern the optimal model. The difference in Bayesian evidence ($|\Delta \ln \mathcal{Z}|$) between any two models guided the decision-making process, with a threshold of $|\Delta \ln \mathcal{Z}| > 5$ signifying a significant preference, $|\Delta \ln \mathcal{Z}| > 2.5$ indicating moderate favorability, and values ≤ 2.5 suggesting models as being “indistinguishable,” thus favoring simpler models. Given the presence of significant peaks in the RV data at 8.15 d and around 41 d, we designated the 2cp model as the baseline for comparison. Details of the different models and their Bayesian evidence are presented in Table 5.

While modeling the RV peaks with circular (cp) or Keplerian (ep) orbits, we consistently observed a preference for cp models over ep models. When considering long-term trends in the data, the 1cp model demonstrated moderate favorability over the 2cp model, with a linear trend significantly outperforming a quadratic trend for the 1cp model. The linear trend in the data indicates radial acceleration of the system with a value of -0.017 ± 0.002 m s⁻¹ day⁻¹. If this acceleration is due to a third body in the system, as is outlined in Smith et al. (2017) and related references, the inferred planet would have a mass exceeding 3 M_J and an orbital separation within 4 AU. However, the current observational time baseline is insufficient to confirm its existence.

The subtraction of the first primary signal seen in the GLS periodogram leaves us with the presence of multiple peaks in the RV data. These periods have an overlapping range with the periods observed for the activity indicators within the range of 34 and 50 d. As in Sect. 4.1.1, where GPs are incorporated to compute the photometrically derived rotational period of the star, we

believe that similar quasi-periodic variations are causing residual peaks in the RV data. We thereby employed the QP kernel, similarly, to capture complex periodic signals induced by stellar spots on the surface (Dumusque et al. 2011; Haywood et al. 2014). These signals show their presence not only in the light curve data but also affect certain stellar lines more than others. This results in line shape variations and similar effects showing peaks in the RV data that can be misinterpreted as a planetary signal. We used GP as a tool to model these complex periodic signals. For the GP parameters, we used uniform priors for the GP amplitude ($\sigma_{\text{GP,RV}}$) between 0 and 100 m s^{-1} . The inverse length scale of the external parameter ($\alpha_{\text{GP,RV}}$) and the amplitude of the sine part of the kernel ($\gamma_{\text{GP,RV}}$) had a log uniform distribution between 10^{-10} to 1 and between 0.01 to 10, respectively. We kept the rotational period of the GP ($P_{\text{rot,GP,RV}}$) varying uniformly between 30 to 60 d to account for the additional peaks seen in the RV data that overlap with some signals seen in the activity indicators. The analyses resulted in the 1cp+GP model exhibiting the lowest $\ln \mathcal{Z}$ and a significant distinction from our fiducial 2cp model, establishing it as the optimal solution.

4.2.3. Joint modeling of the RV and transit data

Simultaneous modeling of both RV and transit data facilitates a more precise constraint on the planet and orbital parameters. For instance, parameters such as the orbital period (P) and transit center time (T_c) are influenced by both datasets and are best determined when modeled jointly. In our analysis of the TOI-3493 system, we employed both HARPS RV data and TESS light curves for joint modeling.

The priors used in this joint modeling step were the same as the ones discussed in the previous individual modeling steps, in Sects. 4.2.1 and 4.2.2. These priors are detailed in Table A.1. Notably, the RV semi-amplitude (K) for the planet was determined to be $2.81^{+0.36}_{-0.37} \text{ m s}^{-1}$.

The posterior distribution of the planet parameters resulting from the joint orbital fit are summarized in Tables 6 and 7. Furthermore, a covariance plot illustrating the fit parameters is presented in Fig. A.1. Analysis of the posterior parameters obtained from our joint fit, along with the RV model depicted in Fig. 9, reveals that the maximum posteriori of the GP periodic component, $P_{\text{rot,GP,RV}}$, is $37.44^{+2.09}_{-1.07}$ d, with aliases observed at 34 and 41 d, as is seen in Fig. 7. The best-fit results obtained from joint modeling are visualized in Figs. 2 and 3 for transits and Fig. 9 for RVs.

5. Discussion

5.1. The mass-radius diagram

We derive the bulk density of TOI-3493 b as $1.47^{+0.23}_{-0.22} \text{ g cm}^{-3}$ based on the mass and radius obtained from our analysis (Sect. 4.2.3). Placing TOI-3493 b on the mass-radius (M-R) diagram, depicted in Fig. 10, we compare it with other transiting planets sourced from the Exoplanet Archive¹⁰. These planets are color-coded according to their host stellar temperatures. The solid and dashed lines represent models from Zeng et al. (2019). We consider simplistic models using an H_2 envelope, and a core composed of H_2O and silicates of varying consistencies.

Two different models can best explain the position of TOI-3493 b on the M-R diagram:

Table 6. Posterior parameters of the joint fit for TOI-3493 b.

Parameter ^(a)	TOI-3493 b
P (d)	$8.1594667^{+0.0000016}_{-0.0000017}$
T_0 (BJD)	$2459313.0467455^{+0.0012477}_{-0.0012398}$
a/R_\star	$14.07^{+0.31}_{-0.49}$
$b = (a/R_\star) \cos i_p$	$0.18^{+0.13}_{-0.12}$
i_p (deg)	$89.25^{+0.50}_{-0.59}$
r_1	$0.455^{+0.089}_{-0.081}$
r_2	$0.0240^{+0.0005}_{-0.0006}$
K (m s^{-1})	$2.81^{+0.36}_{-0.37}$
<i>Derived physical parameters</i>	
M (M_\oplus)	$8.97^{+1.17}_{-1.20}$
R (R_\oplus)	$3.22^{+0.08}_{-0.08}$
g (cm s^{-2})	$8.47^{+1.19}_{-1.21}$
ρ (g cm^{-3})	$1.47^{+0.23}_{-0.22}$
S (S_\oplus)	245^{+18}_{-13}
T_{eq} (K) ^(b)	1102^{+20}_{-14}

Notes. ^(a)Parameters obtained with the posterior values from Table 7. Error bars denote the 68% posterior credibility intervals. ^(b)The equilibrium temperature was calculated assuming zero Bond albedo.

Table 7. Posterior distributions of the juliet joint fit for the instrumental and GP fit parameters obtained for the TOI-3493 system.

Parameter ^(a)	TOI-3493
<i>Stellar parameters</i>	
ρ_\star (g cm^{-3})	$0.790^{+0.053}_{-0.079}$
<i>Photometry parameters</i>	
$M_{\text{TESS}37}$ (10^{-6})	$-21^{+4.19}_{-4.22}$
$\sigma_{\text{TESS}37}$ (ppm)	$145^{+10.54}_{-11.27}$
$q_{1,\text{TESS}37}$	$0.61^{+0.23}_{-0.22}$
$q_{2,\text{TESS}37}$	$0.54^{+0.27}_{-0.26}$
$M_{\text{TESS}64}$ (10^{-6})	$-54^{+4.8}_{-4.7}$
$\sigma_{\text{TESS}64}$ (ppm)	$287^{+6.7}_{-6.6}$
$q_{1,\text{TESS}64}$	$0.31^{+0.28}_{-0.19}$
$q_{2,\text{TESS}64}$	$0.29^{+0.23}_{-0.19}$
M_{LCO} (10^{-6})	115^{+54}_{-53}
σ_{LCO} (ppm)	901^{+45}_{-43}
$q_{1,\text{LCO}}$	$0.26^{+0.21}_{-0.19}$
$q_{2,\text{LCO}}$	$0.42^{+0.35}_{-0.29}$
<i>RV parameters</i>	
μ_{HARPS} (m s^{-1})	$-2.29^{+4.9}_{-3.69}$
σ_{HARPS} (m s^{-1})	$1.6^{+0.32}_{-0.36}$
$\dot{\gamma}$ ($\text{m s}^{-1}\text{day}^{-1}$)	-0.017 ± 0.002
<i>GP hyperparameters</i>	
$\sigma_{\text{GP,RV}}$ (m s^{-1})	$7.47^{+7.14}_{-3.38}$
$\alpha_{\text{GP,RV}}$ (10^{-6} d^{-2})	$7.3^{+30.3}_{-6.74}$
$\Gamma_{\text{GP,RV}}$	$0.31^{+2.1}_{-0.28}$
$P_{\text{rot,GP,RV}}$ (d)	$37.44^{+2.09}_{-1.07}$

Notes. ^(a)Priors and descriptions for each parameter are in Table A.1. Error bars denote the 68% posterior credibility intervals.

¹⁰ <https://exoplanetarchive.ipac.caltech.edu>

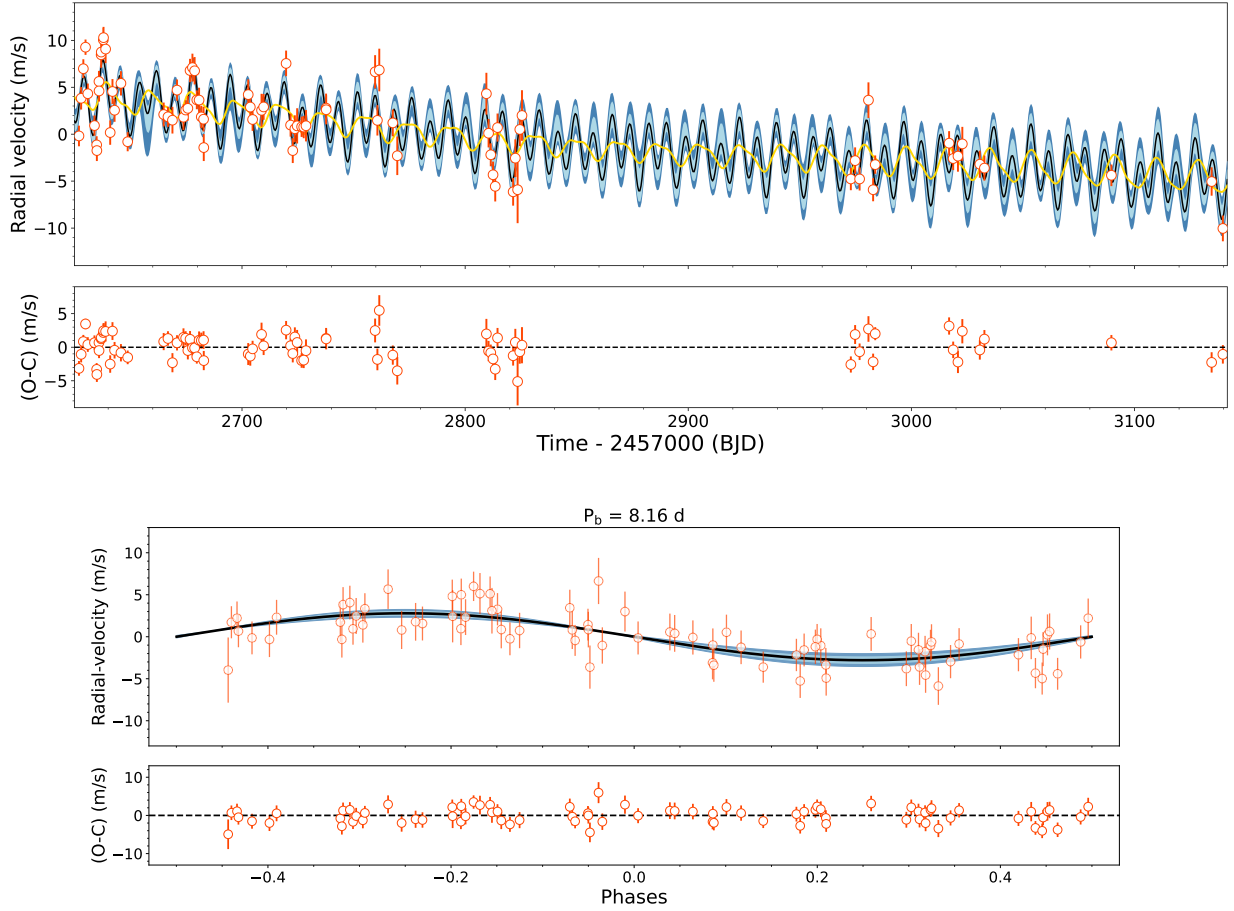


Fig. 9. Joint modeling of the RV data from HARPS (orange) for TOI-3493 along with their residuals. The solid curve is the median best-fit `juliet` model. The shaded light and dark blue regions represent 68% and 95% credibility bands. *Top panel:* RV time-series with the GP component (solid yellow curve). *Bottom panel:* phase-folded RVs for TOI-3493 for the 8.15 d-period planet along with the residuals folded at its period.

1. Assuming a planetary equilibrium temperature of ~ 1000 K (Table 6), we can consider the planetary core to consist of a 99.7% Earth-like composition, with a rocky core of iron and silicates, and water in a 1:1 ratio, and the remaining 0.3% comprising a hydrogen envelope.

2. Alternatively, the planetary core could be composed of 98% iron and silicate, with the remaining 2% constituting a hydrogen envelope.

This suggests that the planet may either have a large core predominantly composed of silicates and water with a thinner hydrogen outer layer, or a smaller, denser rocky core with a thicker hydrogen envelope. In theory, many models can explain the position of TOI-3493 b with a larger percentage of water in the core or a larger fraction of H₂ gas in the envelope. What can be concluded from these scenarios is that TOI-3493 b is likely a water-rich planet. Future atmospheric characterization studies can only shed more light on this case.

In recent years, the discovery of small planets with radii ranging from $1\text{--}4 R_{\oplus}$ has been abundant, with little similarities observed with our solar system planets. This distribution exhibits two distinct populations: one peaking around $1.5 R_{\oplus}$, termed super-Earths, and the other around $2.2 R_{\oplus}$, known as sub-Neptunes. The relative absence of planets between these peaks is referred to as the radius gap (Fulton et al. 2017; Van Eylen et al. 2018; Berger et al. 2018).

Theories such as photo-evaporation (Owen & Wu 2013; López & Fortney 2013) and core-powered mass loss

(Ginzburg et al. 2018; Gupta & Schlichting 2019) have been proposed to explain the radius gap, assuming similar initial planet compositions for both super-Earths and mini-Neptunes. While super-Earths lose their primordial atmospheres over time, leaving behind denser cores, mini-Neptunes retain their outer atmospheres. Léger et al. (2004) proposed an alternative model for mini-Neptune compositions, suggesting that their cores consist of an equal mixture of silicates and ice, known as ocean worlds or water worlds. This alternative composition can explain how planets with equally massive cores may have larger radii and lower densities, affecting their position on the M-R diagram (Luque & Pallé 2022). Consequently, models for the mini-Neptune population exhibit degeneracy. Studying planetary atmospheres, such as detecting hydrogen and helium in transmission spectroscopy or water molecules with JWST, could help resolve this degeneracy. Additionally, the radius gap may depend on the stellar age and evolve over millions of years to gigayears, particularly for models with hydrogen and helium in their outer envelopes, which cool over time due to their low molecular weight. In contrast, water worlds, composed of ice and silicates, may undergo less drastic evolution on similar timescales (Rogers et al. 2023; Fernandes et al. 2022).

5.2. TOI-3493 b in the context of other exoplanets

In Fig. 11, we present a scatter plot illustrating the relationship between the bulk density (ρ) and the equilibrium surface

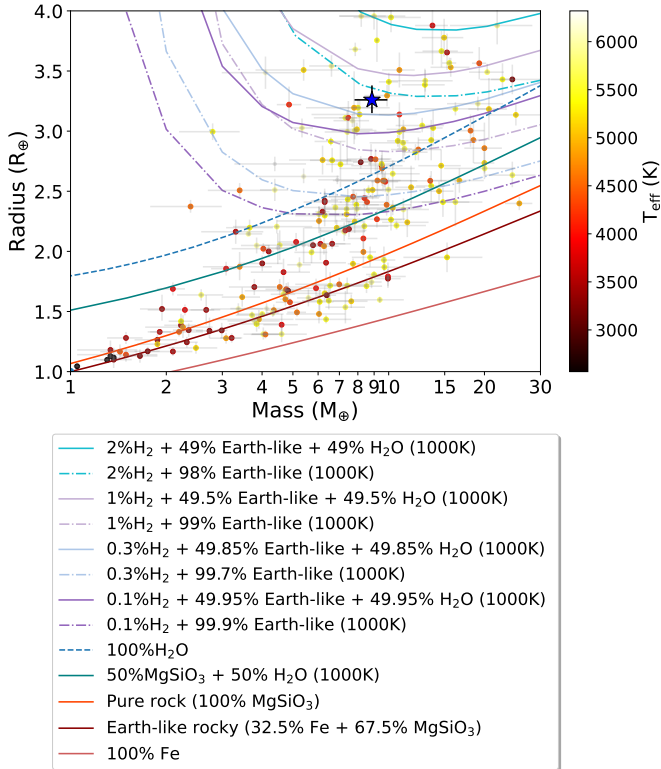


Fig. 10. Mass-radius diagram of well-characterized planets (that have masses and radii characterized with a precision better than 30% and 10%, respectively) with radii of $R < 4R_{\oplus}$ taken from the Transiting Extrasolar Planet Catalogue (Southworth 2011). The planets are color-coded based on the host stellar temperature, from hot (yellow) to cold (red). Theoretical M-R relations are taken from Zeng et al. (2019). TOI-3493 b is marked with a blue star.

temperature (T_{eq}) of small planets with radii, R_p , ranging from 1 to $4.0 R_{\oplus}$. Notably, we include planets with actual mass measurements rather than solely relying on their $m \sin i$ values. The color scheme of the data points corresponds to the temperature of their host stars. We notice from the plot that ρ increases with T_{eq} , a consequence of the high irradiation at high T_{eq} evaporating away the less dense planets so that one ends up preferentially observing remnant cores or high mean molecular weight atmospheres.

The concentration of planets becomes denser from the top to the bottom of the plot. Specifically, the lower region, with planet densities roughly below $1 \rho_{\oplus}$, predominantly comprises mini-Neptunes characterized by outer atmospheres, while the upper region encompasses super-Earths or terrestrial planets.

Solar-type stars exhibit a broad distribution of planets across all density ranges, whereas M dwarf stars tend to host a higher proportion of terrestrial planets compared to mini-Neptunes, which has also been confirmed in studies by Dressing & Charbonneau (2015); Mulders et al. (2015). A distinctive fork-shaped pattern is evident in the distribution of terrestrial planets in Fig. 11. Planets orbiting M dwarfs are predominantly situated on the left side of the fork, reflecting their lower surface temperatures caused by reduced stellar insolation compared to those orbiting solar-type stars. Most stars on the right side of the fork have inflated radii, resulting in lower densities compared to M dwarf exoplanets with similar temperatures. TOI-3493 b, which orbits a G-type star, is located on the right side of the fork. Given its density, which is consistent with that of Neptune, it is hotter

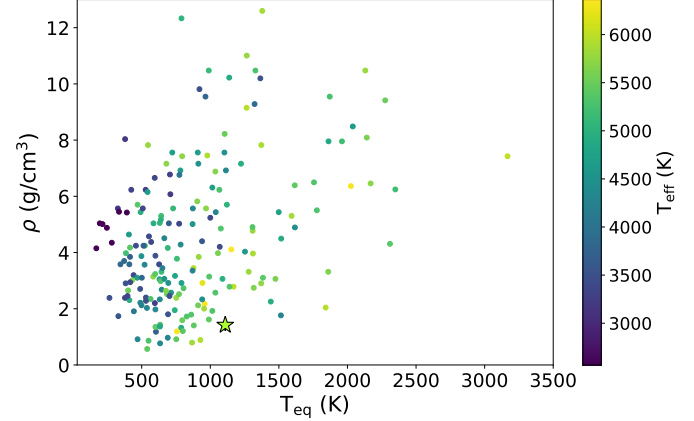


Fig. 11. Planet bulk density as a function of average equilibrium surface temperature of the planet taken from the exoplanet catalog (Southworth 2011). The planets are color-coded based on the host stellar temperature, from hot (yellow) to cold (blue). The position of TOI-3493 b is marked with a star.

than any exoplanet of similar density around a cooler host star. The cluster of planets on the left side of the fork suggests a population exhibiting a weak dependence on equilibrium temperature relative to bulk density. The upper left grouping may consist of similar planets that have undergone atmospheric stripping, potentially due to XUV irradiation during their early evolution as was discussed previously in this paper, which is particularly relevant for small planets orbiting M dwarfs, which emit XUV radiation during their initial 100 Myr. Analogous planets around solar-type stars are expected to have larger planetary cores or their outer envelopes scaled with respect to the stellar host mass, making them on average less dense than their M-dwarf counterparts for similar temperatures (Petigura et al. 2022). Thus, many of these are located on the right side of the fork.

5.3. Prospects for atmospheric characterization

Recently, Hord et al. (2024) presented a sample of TESS planets and planet candidates optimal for transmission and emission spectroscopy with JWST in a given range of planetary sizes and equilibrium temperatures. All planets were divided into grids with bins in equilibrium temperature (T_{eq}) from 100 to 3000 K ((100–350) K, (350–800) K, (800–1250) K, (1250–1750) K, (1750–2250) K, and (2250–3000) K) and planetary radius (R_p) from 0.3 to $25.0 R_{\oplus}$ ((0.3–1.5) R_{\oplus} , (1.5–2.75) R_{\oplus} , (2.75–4.00) R_{\oplus} , (4–10) R_{\oplus} , and (10–25) R_{\oplus}) to identify the top planets and planet candidates ranked by the transmission spectroscopy metric (TSM) in each bin. This is justified by the fact that the TSM, as it is defined by Kempton et al. (2018), Eq. (1), is proportional to the planet’s equilibrium temperature and the cube of the planet’s radius. Higher equilibrium temperatures and larger planetary radii simply increase the TSM very quickly.

With a radius of $R_b = 3.22 \pm 0.08 R_{\oplus}$, TOI-3493 b belongs to the group of large sub-Neptunes that Hord et al. (2024) defined as planets with radii between 2.75 and $4.0 R_{\oplus}$. With $T_{\text{eq}} = 1102^{+20}_{-14}$ K, TOI-3493 b is located close to the border of two ranges of equilibrium temperature defined by Hord et al. (2024) between 800 K and 1250 K and between 1250 K and 1750 K. Therefore, in Fig. 12 we present all TESS large sub-Neptunes and planetary candidates from the above two groups of equilibrium temperatures. As is shown in Fig. 12, TOI-3493 b has a

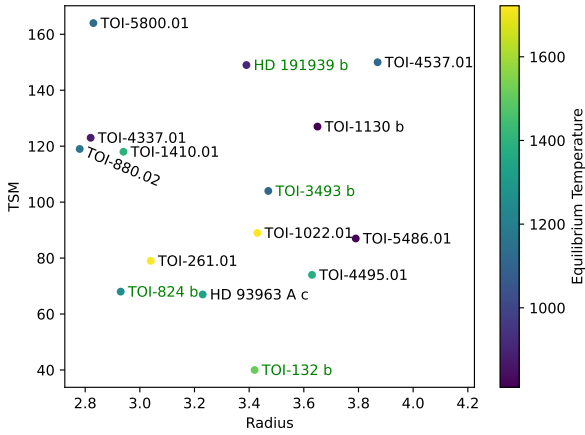


Fig. 12. TSM versus planet radius for hot ($800 \text{ K} < T_{\text{eq}} < 1750 \text{ K}$) large sub-Neptunes ($2.75 < R_p < 4.0 R_{\oplus}$). TOI-3493 b is the second-most promising sub-Neptune along with three others (all marked in green) for transmission spectroscopy studies in the given temperature range and with mass measurement precisions exceeding 5σ discussed in the text. Data come from Hord et al. (2024). The names of the confirmed planets with mass measurements $>5\sigma$ are in green.

TSM of approximately 110, making it the second-most favorable target for transmission spectroscopy studies, among the four confirmed sub-Neptunes with mass measurement precisions exceeding 5σ , highlighted with names in green font in the figure (with HD 191939 b being the most favorable among them).

6. Summary

The TOI-3493 system comprises an early G-type star with a transiting sub-Neptune in a circular orbit. The host star has a surface temperature of $T_{\text{eff}} = 5844 \pm 42 \text{ K}$, surface gravity of $\log g = 4.25 \pm 0.06 \text{ dex}$, and metallicity of $[\text{Fe}/\text{H}] = 0.03 \pm 0.04 \text{ dex}$. We thereby determine a stellar mass of $1.023 \pm 0.041 M_{\odot}$ and a stellar radius of $1.228 \pm 0.017 R_{\odot}$.

The relatively bright star ($G = 9.127 \text{ mag}$) is located at a distance of $96.76 \pm 0.2 \text{ pc}$. We also determine that the star is inactive, with a rotational period of around 34 d.

The system consists of a transiting sub-Neptune that has a mass of $M = 8.97^{+1.17}_{-1.20} M_{\oplus}$, a radius of $R = 3.22 \pm 0.08 R_{\oplus}$, and an orbital period of 8.15 d. The bulk density of the planet is $1.47^{+0.23}_{-0.22} \text{ g cm}^{-3}$, which is consistent with a Neptune-like density. TOI-3493 b is a promising candidate for transmission spectroscopy measurements for exoplanets, placed second to HD 191939 b on the metric scale.

Data availability

Table B.1 is available in electronic form at the CDS via anonymous ftp to cdsarc.cds.unistra.fr (130.79.128.5) or via <https://cdsarc.cds.unistra.fr/viz-bin/cat/J/A+A/697/A169>

Acknowledgements. PC acknowledges the support of the Department of Atomic Energy, Government of India and the financial support from the Thüringer Ministerium für Wirtschaft. The research is partly supported by Deutsche Forschungsgemeinschaft (DFG) grant CH 2636/1-1. The spectroscopy observations were performed with the 3.6 m telescope at the European Southern Observatory (La Silla, Chile) under programs 1102.C-0923 and 106.21TJ.001. Funding for the TESS mission is provided by NASA’s Science Mission Directorate. We acknowledge the use of public TESS data from pipelines at the TESS Science Office and at the TESS Science Processing Operations Center. This research has made use of the Exoplanet Follow-up Observation Program website, which is operated by the

California Institute of Technology, under contract with the National Aeronautics and Space Administration under the Exoplanet Exploration Program. Resources supporting this work were provided by the NASA High-End Computing (HEC) Program through the NASA Advanced Supercomputing (NAS) Division at Ames Research Center for the production of the SPOC data products. This paper includes data collected by the TESS mission that are publicly available from the Mikulski Archive for Space Telescopes (MAST). This work makes use of observations from the LCOGT network. Part of the LCOGT telescope time was granted by NOIRLab through the Mid-Scale Innovations Program (MSIP). MSIP is funded by NSF. Funding for the TESS mission is provided by NASA’s Science Mission Directorate. Some of the Observations in the paper made use of the High-Resolution Imaging instrument. ‘Alopeke. ‘Alopeke was funded by the NASA Exoplanet Exploration Program and built at the NASA Ames Research Center by Steve B. Howell, Nic Scott, Elliott P. Horch, and Emmett Quigley. Data were reduced using a software pipeline originally written by Elliott Horch and Mark Everett. ‘Alopeke was mounted on the Gemini North telescope of the international Gemini Observatory, a program of NSF’s OIR Lab, which is managed by the Association of Universities for Research in Astronomy (AURA) under a cooperative agreement with the National Science Foundation, on behalf of the Gemini partnership: the National Science Foundation (United States), National Research Council (Canada), Agencia Nacional de Investigación y Desarrollo (Chile), Ministerio de Ciencia, Tecnología e Innovación (Argentina), Ministério da Ciência, Tecnologia, Inovações e Comunicações (Brazil), and Korea Astronomy and Space Science Institute (Republic of Korea). Data were partly collected with the LCOGT network (part of the LCOGT telescope time was granted by NOIRLab through the Mid-Scale Innovations Program (MSIP), which is funded by the National Science Foundation). G.N. thanks for the research funding from the Ministry of Education and Science programme the ‘‘Excellence Initiative – Research University’’ conducted at the Centre of Excellence in Astrophysics and Astrochemistry of the Nicolaus Copernicus University in Toruń, Poland. G.N. also thanks the Centre of Informatics Tricity Academic Supercomputer and network (CI TASK, Gdańsk, Poland) for providing computing resources (grant no. PT01187).

References

- Allard, F., Homeier, D., & Freytag, B. 2012, *Philos. Trans. Roy. Soc. Lond. Ser. A*, 370, 2765
- Ambikasaran, S., Foreman-Mackey, D., Greengard, L., Hogg, D. W., & O’Neil, M. 2015, *IEEE Trans. Pattern Anal. Mach. Intell.*, 38, 252
- Anglada-Escudé, G., & Butler, R. P. 2012, *ApJS*, 200, 15
- Angus, R., Morton, T., Aigrain, S., Foreman-Mackey, D., & Rajpaul, V. 2018, *MNRAS*, 474, 2094
- Arenou, F., Luri, X., Babusiaux, C., et al. 2018, *A&A*, 616, A17
- Baglin, A., Auvergne, M., Boisnard, L., et al. 2006, in *36th COSPAR Scientific Assembly*, 36, 3749
- Baranne, A., Queloz, D., Mayor, M., et al. 1996, *A&AS*, 119, 373
- Batalha, N. M., Rowe, J. F., Bryson, S. T., et al. 2013, *ApJS*, 204, 24
- Berger, T. A., Huber, D., Gaidos, E., & van Saders, J. L. 2018, *ApJ*, 866, 99
- Borucki, W. J., Koch, D., Basri, G., et al. 2010, *Science*, 327, 977
- Brown, T. M., Baliber, N., Bianco, F. B., et al. 2013, *PASP*, 125, 1031
- Bruntt, H., De Cat, P., & Aerts, C. 2008, *A&A*, 478, 487
- Butters, O. W., West, R. G., Anderson, D. R., et al. 2010, *A&A*, 520, L10
- Cannon, A. J., & Pickering, E. C. 1920, *Ann. Harvard Coll. Observ.*, 95, 1
- Castelli, F., & Kurucz, R. L. 2004, astro-ph/0405087 [[astro-ph/0405087](https://arxiv.org/abs/astro-ph/0405087)]
- Catanzarite, J., & Shao, M. 2011, *ApJ*, 738, 151
- Charbonneau, D., Brown, T. M., Latham, D. W., & Mayor, M. 2000, *ApJ*, 529, L45
- Choi, J., Dotter, A., Conroy, C., et al. 2016, *ApJ*, 823, 102
- Ciardi, D. R., Beichman, C. A., Horch, E. P., & Howell, S. B. 2015, *ApJ*, 805, 16
- Collins, K. 2019, in *American Astronomical Society Meeting Abstracts*, 233, 140.05
- Collins, K. A., Kielkopf, J. F., Stassun, K. G., & Hessman, F. V. 2017, *AJ*, 153, 77
- Cumming, A., Butler, R. P., Marcy, G. W., et al. 2008, *PASP*, 120, 531
- Doyle, A. P., Davies, G. R., Smalley, B., Chaplin, W. J., & Elsworth, Y. 2014, *MNRAS*, 444, 3592
- Dressing, C. D., & Charbonneau, D. 2015, *ApJ*, 807, 45
- Dumusque, X., Udry, S., Lovis, C., Santos, N. C., & Monteiro, M. J. P. F. G. 2011, *A&A*, 525, A140
- Espinoza, N. 2018, *AAS*, 2, 209
- Espinoza, N., Kossakowski, D., & Brahm, R. 2019, *MNRAS*, 490, 2262
- Fernandes, R., Mulders, G., Pascucci, I., Bergsten, G., & Koskinen, T. 2022, in *Bulletin of the American Astronomical Society*, 54, 102.47
- Fischer, D. A., Laughlin, G., Butler, P., et al. 2005, *ApJ*, 620, 481
- Foreman-Mackey, D., Agol, E., Ambikasaran, S., & Angus, R. 2017, *celerite: Scalable 1D Gaussian Processes in C++, Python, and Julia*, Astrophysics Source Code Library [[record asc:1709.008](https://arxiv.org/abs/record%20asc%3A%2F1709.008)]

- Fulton, B. J., Petigura, E. A., Howard, A. W., et al. 2017, *AJ*, **154**, 109
- Fulton, B. J., Petigura, E. A., Blunt, S., & Sinukoff, E. 2018, *PASP*, **130**, 044504
- Gaia Collaboration 2020, VizieR Online Data Catalog: I/350
- Gaia Collaboration (Brown, A. G. A., et al.) 2021, *A&A*, **649**, A1
- Ginzburg, S., Schlichting, H. E., & Sari, R. 2018, *MNRAS*, **476**, 759
- Guerrero, N. M., Seager, S., Huang, C. X., et al. 2021, *ApJS*, **254**, 39
- Gupta, A., & Schlichting, H. E. 2019, *MNRAS*, **487**, 24
- Gupta, A., & Schlichting, H. E. 2020, *MNRAS*, **493**, 792
- Haywood, R. D., Collier Cameron, A., Queloz, D., et al. 2014, *MNRAS*, **443**, 2517
- Hord, B. J., Kempton, E. M. R., Evans-Soma, T. M., et al. 2024, *AJ*, **167**, 233
- Houk, N., & Smith-Moore, M. 1988, *Michigan Catalogue of Two-dimensional Spectral Types for the HD Stars. Declinations*
- Howard, A. W., Johnson, J. A., Marcy, G. W., et al. 2010, *ApJ*, **721**, 1467
- Howard, A. W., Marcy, G. W., Bryson, S. T., et al. 2012, *ApJS*, **201**, 15
- Howell, S. B., & Furlan, E. 2022, *Front. Astron. Space Sci.*, **9**, 871163
- Howell, S. B., Everett, M. E., Sherry, W., Horch, E., & Ciardi, D. R. 2011, *AJ*, **142**, 19
- Howell, S. B., Matson, R. A., Ciardi, D. R., et al. 2021, *AJ*, **161**, 164
- Husser, T. O., Wende-von Berg, S., Dreizler, S., et al. 2013, *A&A*, **553**, A6
- Jenkins, J. M. 2002, *ApJ*, **575**, 493
- Jenkins, J. M., Chandrasekaran, H., McCauliff, S. D., et al. 2010, *SPIE Conf. Ser.*, **7740**, 77400D
- Jenkins, J. M., Twicken, J. D., McCauliff, S., et al. 2016, *Proc. SPIE*, **9913**, 99133E
- Jenkins, J. M., Tenenbaum, P., Seader, S., et al. 2020, *Kepler Data Processing Handbook: Transiting Planet Search*, Kepler Science Document KSCI-19081-003
- Kempton, E. M. R., Bean, J. L., Louie, D. R., et al. 2018, *PASP*, **130**, 114401
- Kreidberg, L. 2015, *PASP*, **127**, 1161
- Kreidberg, L. 2018, in *Handbook of Exoplanets*, eds. H. J. Deeg, & J. A. Belmonte, 100
- Kurucz, R. L. 1993, VizieR Online Data Catalog: VI/39
- Kurucz, R. L. 2013, ATLAS12: Opacity sampling model atmosphere program, Astrophysics Source Code Library [record ascl:1303.024]
- Léger, A., Selsis, F., Sotin, C., et al. 2004, *Icarus*, **169**, 499
- Lester, K. V., Matson, R. A., Howell, S. B., et al. 2021, *AJ*, **162**, 75
- Li, J., Tenenbaum, P., Twicken, J. D., et al. 2019, *PASP*, **131**, 024506
- Lindgren, L., Hernández, J., Bombrun, A., et al. 2018, *A&A*, **616**, A2
- López, E. D., & Fortney, J. J. 2013, *ApJ*, **776**, 2
- Lovis, C., & Pepe, F. 2007, *A&A*, **468**, 1115
- Luque, R., & Pallé, E. 2022, *Science*, **377**, 1211
- Mamajek, E. E., & Hillenbrand, L. A. 2008, *ApJ*, **687**, 1264
- Marcy, G., Butler, R. P., Fischer, D., et al. 2005, *Progr. Theor. Phys. Suppl.*, **158**, 24
- Matson, R. A., Howell, S. B., Horch, E. P., & Everett, M. E. 2018, *AJ*, **156**, 31
- Mayor, M., Pepe, F., Queloz, D., et al. 2003, *The Messenger*, **114**, 20
- Mayor, M., Marmier, M., Lovis, C., et al. 2011, arXiv e-prints [arXiv:1109.2497]
- McCully, C., Volgenau, N. H., Harbeck, D.-R., et al. 2018, *SPIE Conf. Ser.*, **10707**, 107070K
- Mulders, G. D., Pascucci, I., & Apai, D. 2015, *ApJ*, **798**, 112
- Owen, J. E., & Wu, Y. 2013, *ApJ*, **775**, 105
- Pepe, F., Mayor, M., Galland, F., et al. 2002, *A&A*, **388**, 632
- Persson, C. M., Fridlund, M., Barragán, O., et al. 2018, *A&A*, **618**, A33
- Petigura, E. A., Rogers, J. G., Isaacson, H., et al. 2022, *AJ*, **163**, 179
- Piskunov, N., & Valenti, J. A. 2017, *A&A*, **597**, A16
- Ricker, G. R., Winn, J. N., Vanderspek, R., et al. 2015, *J. Astron. Telesc. Instrum. Syst.*, **1**, 014003
- Rogers, J. G., Schlichting, H. E., & Owen, J. E. 2023, *ApJ*, **947**, L19
- Ryabchikova, T., Piskunov, N., Kurucz, R. L., et al. 2015, *Phys. Scr.*, **90**, 054005
- Sanz-Forcada, J., Micela, G., Ribas, I., et al. 2011, *A&A*, **532**, A6
- Schlegel, D. J., Finkbeiner, D. P., & Davis, M. 1998, *ApJ*, **500**, 525
- Scott, N. J., Howell, S. B., Gnilka, C. L., et al. 2021, *Front. Astron. Space Sci.*, **8**, 138
- Smith, J. C., Stumpe, M. C., Van Cleve, J. E., et al. 2012, *PASP*, **124**, 1000
- Smith, A. M. S., Gandolfi, D., Barragán, O., et al. 2017, *MNRAS*, **464**, 2708
- Southworth, J. 2011, *MNRAS*, **417**, 2166
- Sozzetti, A., Torres, G., Charbonneau, D., et al. 2007, *ApJ*, **664**, 1190
- Speagle, J. S. 2020, *MNRAS*, **493**, 3132
- Stassun, K. G., Oelkers, R. J., Pepper, J., et al. 2018, *AJ*, **156**, 102
- Stassun, K. G., Oelkers, R. J., Paegert, M., et al. 2019, *AJ*, **158**, 138
- Stumpe, M. C., Smith, J. C., Van Cleve, J. E., et al. 2012, *PASP*, **124**, 985
- Stumpe, M. C., Smith, J. C., Catanzarite, J. H., et al. 2014, *PASP*, **126**, 100
- Tokovinin, A. 2018, *PASP*, **130**, 035002
- Trotta, R. 2008, *Contemp. Phys.*, **49**, 71
- Twicken, J. D., Catanzarite, J. H., Clarke, B. D., et al. 2018, *PASP*, **130**, 064502
- Valenti, J. A., & Piskunov, N. 1996, *A&AS*, **118**, 595
- Van Eylen, V., Agentoft, C., Lundkvist, M. S., et al. 2018, *MNRAS*, **479**, 4786
- Van Eylen, V., Astudillo-Defru, N., Bonfils, X., et al. 2021, *MNRAS*, **507**, 2154
- Vines, J. I., & Jenkins, J. S. 2022, *MNRAS*, **513**, 2719
- Yee, S. W., Petigura, E. A., & von Braun, K. 2017, *ApJ*, **836**, 77
- Zechmeister, M., & Kürster, M. 2009, *A&A*, **496**, 577
- Zeng, L., Jacobsen, S. B., & Sasselov, D. D. 2017, *RNAAS*, **1**, 32
- Zeng, L., Jacobsen, S. B., Sasselov, D. D., et al. 2019, *PNAS*, **116**, 9723
- Ziegler, C., Tokovinin, A., Briceño, C., et al. 2020, *AJ*, **159**, 19

-
- 1 Thüringer Landessternwarte Tautenburg, Sternwarte 5, 07778 Tautenburg, Germany
 - 2 Department of Astronomy and Astrophysics, Tata Institute of Fundamental Research, Mumbai 400005, India
 - 3 Dipartimento di Fisica, Università degli Studi di Torino, via Pietro Giuria 1, 10125 Torino, Italy
 - 4 Department of Space, Earth and Environment, Chalmers University of Technology, Onsala Space Observatory, 43992 Onsala, Sweden
 - 5 Institute of Astronomy, Faculty of Physics, Astronomy and Informatics, Nicolaus Copernicus University, Grudziądzka 5, 87-100 Toruń, Poland
 - 6 Space Research Institute, Austrian Academy of Sciences, Schmiedlstrasse 6, 8042 Graz, Austria
 - 7 Center for Astrophysics | Harvard & Smithsonian, 60 Garden Street, Cambridge, MA 02138, USA
 - 8 McDonald Observatory, The University of Texas, Austin, TX, USA
 - 9 Center for Planetary Systems Habitability, The University of Texas, Austin, TX, USA
 - 10 Caltech/IPAC, Mail Code 100-22, Pasadena, CA 91125, USA
 - 11 NASA Ames Research Center, Moffett Field, CA 94035, USA
 - 12 Lund Observatory, Division of Astrophysics, Department of Physics, Lund University, Box 118, 22100 Lund, Sweden
 - 13 Astrobiology Center, 2-21-1 Osawa, Mitaka, Tokyo 181-8588, Japan
 - 14 National Astronomical Observatory of Japan, 2-21-1 Osawa, Mitaka, Tokyo 181-8588, Japan
 - 15 Astronomical Science Program, Graduate University for Advanced Studies, SOKENDAI, 2-21-1, Osawa, Mitaka, Tokyo 181-8588, Japan
 - 16 Instituto de Astrofísica de Canarias (IAC), Calle Vía Láctea s/n, 38205 La Laguna, Tenerife, Spain
 - 17 Departamento de Astrofísica, Universidad de La Laguna (ULL), 38206 La Laguna, Tenerife, Spain
 - 18 Department of Physics and Kavli Institute for Astrophysics and Space Research, Massachusetts Institute of Technology, Cambridge, MA 02139, USA
 - 19 Department of Earth, Atmospheric and Planetary Sciences, Massachusetts Institute of Technology, Cambridge, MA 02139, USA
 - 20 Department of Aeronautics and Astronautics, MIT, 77 Massachusetts Avenue, Cambridge, MA 02139, USA
 - 21 Department of Physics and Astronomy, Vanderbilt University, Nashville, TN 37235, USA
 - 22 SETI Institute, Mountain View, CA 94043, USA/NASA Ames Research Center, Moffett Field, CA 94035, USA
 - 23 Mullard Space Science Laboratory, University College London, Holmbury St Mary, Dorking, Surrey RH5 6NT, UK
 - 24 Department of Astrophysical Sciences, Princeton University, Princeton, NJ 08544, USA
 - 25 Department of Physics, Engineering and Astronomy, Stephen F. Austin State University, 1936 North St, Nacogdoches, TX 75962, USA

Appendix A: Priors and posteriors for data modeling
Table A.1. Priors used for TOI-3493 b in the joint fit with juliet.

Parameter ^a	Prior	Unit	Description
<i>Stellar and planetary parameters</i>			
ρ_*	$\mathcal{U}(100, 10000)$	g cm^{-3}	Stellar density
P	$\mathcal{N}(8.159, 0.002)$	d	Period of planet b
t_0	$\mathcal{N}(2459313.0471, 0.002)$	d	Time of transit center of planet b
r_1	$\mathcal{U}(0, 1)$...	Parameterization for p and b
r_2	$\mathcal{U}(0, 1)$...	Parameterization for p and b
K	$\mathcal{U}(0, 20)$	m s^{-1}	RV semi-amplitude of planet b
e	0.0 (fixed)	...	Orbital eccentricity of planet b
ω	90.0 (fixed)	deg	Periastron angle of planet b
<i>Photometry parameters</i>			
$D_{\text{TESS } 37, 64}$	1.0 (fixed)	...	Dilution factor for TESS sectors 37, 64
$M_{\text{TESS } 37, 64}$	$\mathcal{N}(0, 0.1)$...	Relative flux offset for TESS sectors 37, 64
$\sigma_{\text{TESS } 37, 64}$	$\mathcal{L}\mathcal{U}(10^{-3}, 10^4)$	ppm	Extra jitter term for sectors TESS 37, 64
$q_{1,\text{TESS } 37, 64}$	$\mathcal{U}(0, 1)$...	Limb-darkening parameterization for TESS sectors 37, 64
$q_{2,\text{TESS } 37, 64}$	$\mathcal{U}(0, 1)$...	Limb-darkening parameterization for TESS sectors 37, 64
<i>RV parameters</i>			
μ_{HARPS}	$\mathcal{N}(-10, 10)$	m s^{-1}	RV zero point for HARPS
σ_{HARPS}	$\mathcal{L}\mathcal{U}(0.01, 10)$	m s^{-1}	Extra jitter term for HARPS
$\dot{\gamma}$	$\mathcal{U}(-100, 100)$	$\text{m s}^{-1} \text{day}^{-1}$	Linear trend/Radial acceleration
<i>GP hyperparameters</i>			
$\sigma_{\text{GP,RV}}$	$\mathcal{U}(0, 100)$	m s^{-1}	Amplitude of GP component for the RVs
$\alpha_{\text{GP,RV}}$	$\mathcal{L}\mathcal{U}(10^{-10}, 10^{-6})$	d^{-2}	Inverse length-scale of GP exponential component for the RVs
$\Gamma_{\text{GP,RV}}$	$\mathcal{L}\mathcal{U}(0.1, 10)$...	Amplitude of GP sine-squared component for the RVs
$P_{\text{rot;GP,RV}}$	$\mathcal{U}(10, 60)$	d	Period of the GP QP component for the RVs

Notes. ^(a) $\mathcal{N}(\mu, \sigma^2)$ is a normal distribution of mean μ and variance σ^2 , $\mathcal{U}(a, b)$ and $\mathcal{L}\mathcal{U}(a, b)$ are uniform and log-uniform distributions between a and b .

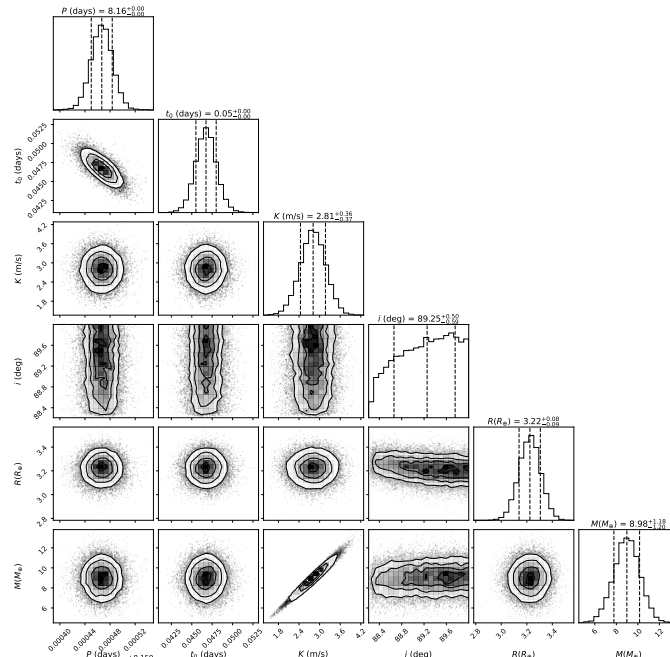


Fig. A.1. Posterior distribution for the joint model parameters (1cp+GP) derived with juliet. The t_0 indicated on this plot is a truncated value ($t_0 - 2459313$) in BJD.